

See discussions, stats, and author profiles for this publication at: <https://www.researchgate.net/publication/258038125>

OH-Initiated Heterogeneous Oxidation of Cholestane: A Model System for Understanding the Photochemical Aging of Cyclic Alkane Aerosols

ARTICLE *in* THE JOURNAL OF PHYSICAL CHEMISTRY A · OCTOBER 2013

Impact Factor: 2.69 · DOI: 10.1021/jp407994m · Source: PubMed

CITATIONS

10

READS

23

8 AUTHORS, INCLUDING:



Christopher R Ruehl

Lawrence Berkeley National Laboratory

31 PUBLICATIONS 322 CITATIONS

SEE PROFILE



Theodora Nah

Georgia Institute of Technology

25 PUBLICATIONS 159 CITATIONS

SEE PROFILE



David Robert Worton

National Physical Laboratory

85 PUBLICATIONS 896 CITATIONS

SEE PROFILE

OH-Initiated Heterogeneous Oxidation of Cholestane: A Model System for Understanding the Photochemical Aging of Cyclic Alkane Aerosols

Haofei Zhang,^{†,‡} Christopher R. Ruehl,[†] Arthur W. H. Chan,^{‡,▽} Theodora Nah,^{†,§} David R. Worton,^{‡,||} Gabriel Isaacman,[‡] Allen H. Goldstein,^{‡,⊥,#} and Kevin R. Wilson^{*,†}

[†]Chemical Sciences Division, Lawrence Berkeley National Laboratory, Berkeley, California 94720, United States

[‡]Department of Environmental Sciences, Policy, and Management, University of California, Berkeley, California 94720, United States

[§]Department of Chemistry, University of California, Berkeley, California 94720, United States

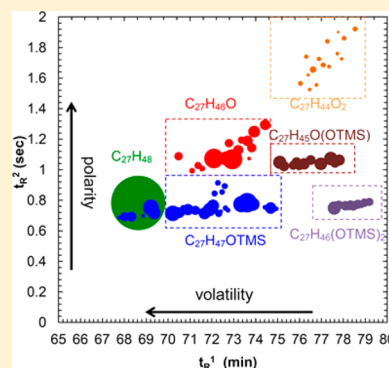
^{||}Aerosol Dynamics Inc., Berkeley, California 94720, United States

[⊥]Environmental and Energy Technologies Division, Lawrence Berkeley National Laboratory, Berkeley, California 94720, United States

[#]Department of Civil and Environmental Engineering, University of California, Berkeley, California 94720, United States

S Supporting Information

ABSTRACT: Aerosols containing aliphatic hydrocarbons play a substantial role in the urban atmosphere. Cyclic alkanes constitute a large fraction of aliphatic hydrocarbon emissions originating from incomplete combustion of diesel fuel and motor oil. In the present study, cholestane ($C_{27}H_{48}$) is used as a model system to examine the OH-initiated heterogeneous oxidation pathways of cyclic alkanes in a photochemical flow tube reactor. Oxidation products are collected on filters and analyzed by a novel soft ionization two-dimensional gas chromatography/mass spectrometry technique. The analysis reveals that the first-generation functionalization products (cholestanones, cholestanals, and cholestanols) are the dominant reaction products that account for up to 70% by mass of the total speciated compounds. The ratio of first-generation carbonyls to alcohols is near unity at every oxidation level. Among the cholestanones/cholestanals, 55% are found to have the carbonyl group on the rings of the androstane skeleton, while 74% of cholestanols have the hydroxyl group on the rings. Particle-phase oxidation products with carbon numbers less than 27 (i.e., “fragmentation products”) and higher-generation functionalization products are much less abundant. Carbon bond cleavage was found to occur only on the side chain. Tertiary-carbon alkoxy radicals are suggested to play an important role in governing both the distribution of functionalization products (via alkoxy radical isomerization and reaction with oxygen) and the fragmentation products (via alkoxy radical decomposition). These results provide new insights into the oxidation mechanism of cyclic alkanes.



1. INTRODUCTION

Atmospheric fine particulate matter ($PM_{2.5}$) plays a significant role in climate change, human health, and air quality.¹ In the urban troposphere, an important fraction of $PM_{2.5}$ is aliphatic hydrocarbons emitted from motor vehicles. These particle-phase hydrocarbons can be oxidized by gas-phase radicals, primarily hydroxyl radicals (OH), to form oxygenated products. These photochemical transformations, often referred to as “chemical aging”, alter the composition and hence other properties of organic aerosols, such as size, hygroscopicity, and optical properties.²

The aging process can proceed via the addition of oxygenated functional groups (i.e., carbonyl and hydroxyl groups) to form lower volatility products (functionalization) or by C–C bond scission to produce higher volatility products (fragmentation).^{3,4} The relative importance of these two oxidative pathways has been observed to be highly dependent

on molecular structure.^{5,6} For gas-phase hydrocarbons, branching of the carbon backbone increases fragmentation, in contrast to rings, which increase functionalization.^{5–7} By comparison, the influence of molecular structure on heterogeneous oxidation has been less studied. OH-initiated heterogeneous oxidation of aerosols is expected to be rather fast at particle surfaces, compared with the slow OH diffusion into solid organics or viscous liquids.⁸ Thus oxidation by OH most likely occurs on the particle surface, which in turn may result in both distinct reaction mechanisms and isomeric distributions of the reaction products not observed for a gas-phase reaction.

Laboratory studies of heterogeneous organic aerosol oxidation have mostly been investigated in flow tube reactors,

Received: August 9, 2013

Revised: October 22, 2013

Published: October 23, 2013



which use high radical concentrations and short reaction times to mimic low radical concentrations and long reaction time in the real atmosphere.^{9–11} An important index of heterogeneous oxidation kinetics is the reactive uptake coefficient (γ), which is the probability that reaction occurs upon a gas–surface collision. Kinetic data obtained from previous studies suggest that heterogeneous oxidation of organic aerosol by OH is efficient, with γ ranging from 0.25 to over 1.^{9–13} Uptake coefficients larger than unity suggest that secondary reactions in the particle phase produce additional loss pathways for reactants. For multicomponent hydrocarbon aerosols, effective uptake coefficients were reported to be in the range 0.5–2, with branched alkanes exhibiting the most rapid kinetics in contrast to cyclic alkanes, which are a factor of ~ 2 slower.¹⁴ OH exposure levels were also found to influence oxidation kinetics, with lower OH exposures yielding higher reactive uptake coefficients.^{11,14–16}

Previous studies have investigated how the bulk properties of organic aerosol change upon photochemical aging by use of aerosol mass spectrometry,^{9,11,13,17–19} yet to date a detailed mechanism of heterogeneous oxidation has not been obtained. One of the main challenges for developing such a mechanism is the need to comprehensively characterize the composition of the oxidation products at a molecular level. A recent study combined two-dimensional gas chromatography with high-resolution vacuum UV photoionization mass spectrometry²⁰ to investigate heterogeneous oxidation of squalane (highly branched alkane) and *n*-octacosane (straight alkane) aerosol.²¹ This technique resolved most of the structural isomers of the oxidation products, providing deeper insight into how molecular structure and aerosol phase state influence heterogeneous reaction pathways. In addition to straight and branched alkanes, cyclic alkanes are also an important component in the urban aerosol, comprising a dominant fraction of primary organic aerosol emitted from on-road motor vehicles.²² In the present work, cholestane ($C_{27}H_{48}$, number of double-bond equivalents $N_{DBE} = 4$), a marker for motor vehicle exhaust¹⁶ is used as a model compound to study the OH-initiated heterogeneous oxidation of cyclic alkanes in a flow tube reactor. Here we report kinetic measurements and a comprehensive analysis of the oxidation products.

2. EXPERIMENTAL SECTION

2.1. Flow Tube Reactor Experiments. An atmospheric pressure flow tube reactor (1.4 m long, 5.8 cm i.d., quartz tube) was used to study the OH-initiated heterogeneous oxidation of cholestane particles. Cholestane particles were formed by homogeneous nucleation in a N_2 stream flowing through a 60-cm-long glass tube containing solid cholestane (5 α -cholestane, Sigma, purity >97%). The aerosol stream was then passed through a thermal denuder in order to optimize the spherical shape of particles. The quartz tube was heated in a tube furnace at 130 °C and the temperature of the thermal denuder was set at 70 °C, producing a log-normal aerosol size distribution with mean surface-weighted diameter of $\sim 210 \pm 10$ nm as measured by a scanning mobility particle sizer (SMPS, TSI Inc.). The total particle mass concentrations were $\sim 2000 \mu\text{g}\cdot\text{m}^{-3}$. The aerosol was then mixed with humidified N_2 , O_2 , and O_3 before entry into the flow tube reactor. The total flow through the flow tube was fixed at $2.0 \text{ L}\cdot\text{min}^{-1}$, corresponding to a residence time of ~ 110 s. The relative humidity was fixed at 30% in the flow tube reactor. O_3 (0–40 ppm) was generated by an O_3 generator (Ozone Solution Inc., HG-1500) and measured by an

O_3 monitor (2B Technologies, Inc.). OH radicals were formed in the flow tube reaction from the reaction of water vapor with $O(^1D)$, produced from ozone photolysis by mercury lamps ($\lambda = 254$ nm, UVP, LLC). The OH concentration in the flow tube was adjusted by controlling the O_3 concentration and was calculated on the basis of the decay of a gas-phase tracer (i.e., hexane) detected by a gas chromatograph (GC, SRI Instruments) as described by Smith et al.¹¹ The OH exposure ranged from 0 to 4×10^{12} molecules $\cdot\text{cm}^{-3}\cdot\text{s}$ in all experiments, equivalent to several weeks' oxidation in the troposphere assuming a 24-h average OH concentration of 1.5×10^6 molecules cm^{-3} .

At each OH oxidation level, aerosol samples were collected for 10 min at a flow rate of $0.6 \text{ L}\cdot\text{min}^{-1}$ on quartz fiber filters (47 mm Tissuquartz, Pall Life Science, prebaked at 600 °C). The sample flow passed through a charcoal denuder (8 in. 480-channel, MAST Carbon) before the filters to minimize positive gas-phase artifacts caused by gas-phase adsorption to the filter media.¹⁴

2.2. Two-Dimensional Gas Chromatography with High-Resolution Time-of-Flight Mass Spectrometry Utilizing either Electron Impact or Vacuum UV Ionization. Filter samples were stored at -20 °C before analysis. Aliquots of each filter ($0.4\text{--}0.8 \text{ cm}^2$) were thermally desorbed (in helium) into a gas chromatograph (Agilent 7890) by use of a Gerstel thermal desorption system with in situ gas-phase derivatization by *N*-methyl-*N*-trimethylsilyl trifluoroacetamide (MSTFA). Analytes were separated by two-dimensional gas chromatography and detected by high-resolution time-of-flight mass spectrometry utilizing either electron impact or vacuum UV ionization (TD-GC \times GC/EL/VUV-HR-TOFMS). Internal standards of deuterated $C_{12}\text{--}C_{36}$ *n*-alkanes were used to correct for transfer efficiency and reproducibility. External standards were also analyzed for quantification purposes.¹⁴ 2-Octadecanone (Sigma–Aldrich, purity >97%), and cholesterol (Sigma–Aldrich, purity >99%) are used as surrogate standards to quantify carbonyl and alcohol products, respectively. The response of 2-octadecanone was corrected by use of the internal standards. A first-dimension nonpolar column ($60 \text{ m} \times 0.25 \text{ mm} \times 0.25 \mu\text{m}$, Rxi-5Sil MS, Restek Corp.) is connected to a second-dimension polar column ($1 \text{ m} \times 0.25 \text{ mm} \times 0.25 \mu\text{m}$, Rtx-200MS, Restek Corp.) by a dual loop modulator ($1.5 \text{ m} \times 0.25 \text{ mm}$ Rxi guard column) that is cooled with refrigerated air from a coldfinger and periodically heated by a pulse of hot air (Zoex Corp.). The first-dimension column separates compounds by volatility (total run time 85 min) while the second-dimension column separates compounds by polarity (modulator frequency 2.3 s). A high-resolution ($m/\Delta m \approx 4000$) time-of-flight mass spectrometer (HR-TOF, Tofwerk) was used with either electron impact (EI) ionization (70 eV) or vacuum-ultraviolet (VUV) photoionization (10.5 eV). The VUV source was provided by the Chemical Dynamics Beamline (9.0.2) at the Advanced Light Source, Lawrence Berkeley National Laboratory. The beamline produces a photon flux of $10^{15}\text{--}10^{16}$ photons $\cdot\text{s}^{-1}$ at ~ 0.2 eV bandwidth and is tunable from approximately 7 to 30 eV. High-resolution peak-fitting was performed for known compounds to guarantee that potential biases and incorrect mass assignments are minimized.¹⁴

3. RESULTS AND DISCUSSION

3.1. Oxidation Kinetics. Figure 1 shows the normalized SMPS particle volume (black triangles) that is observed to decrease as a function of increasing OH exposure. During

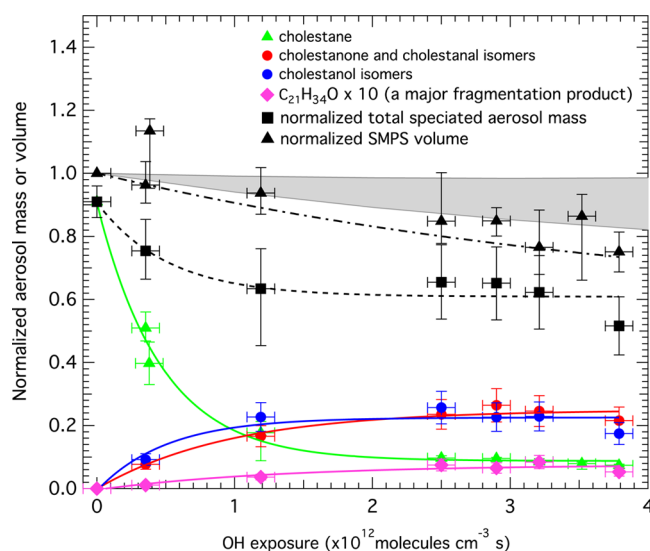


Figure 1. Normalized SMPS total particle volume change as a function of OH exposure (black triangles). The gray area represents the estimated total particle mass if a linear change in density from 0.91 to 1.20 $\text{g}\cdot\text{cm}^{-3}$ is assumed. Also shown are the normalized mass concentrations of cholestane (shown as green triangles), cholestanone/cholestanal isomers (shown as red circles), cholestanol isomers (shown as blue circles), and the dominant fragmentation product (i.e., $\text{C}_{21}\text{H}_{34}\text{O}$, magnified by a factor of 10, shown as pink diamonds) relative to initial cholestane as a function of OH exposure. 2-Octadecanone and cholesterol are used as surrogate standards to quantify carbonyl and alcohol products, respectively. Total speciated aerosol mass is measured by TD-GC \times GC/EI/VUV-HR-TOFMS (black squares).

oxidation, the particle density is expected to change from 0.91 $\text{g}\cdot\text{cm}^{-3}$ for pure cholestane particles to 1.0–1.2 $\text{g}\cdot\text{cm}^{-3}$ for the oxygenated products.^{5,9} Thus the total particle volume data may not be representative of the actual particle mass. The gray area in Figure 1 represents the predicted normalized total aerosol mass, if it is assumed that the bulk particle density linearly changes from 0.91 to 1.0 $\text{g}\cdot\text{cm}^{-3}$ (lower bound) or 1.2

$\text{g}\cdot\text{cm}^{-3}$ (upper bound) at an OH exposure of 4×10^{12} molecules· $\text{cm}^{-3}\cdot\text{s}^{-1}$ (see Supporting Information). The particle shape factor may also change during oxidation (from irregular shape to spherical particles).²¹ However, since a thermal denuder was used to optimize the spherical shape of particles prior to introduction into the flow tube, any change in the particle shape factor is assumed to be negligible.

The decay of cholestane (normalized to the initial total particle mass) at each OH exposure (green triangles) is obtained from the TD-GC \times GC/EI-HR-TOFMS measurements using total EI signals and two most prominent EI fragments (i.e., m/z 217 and 357; see Supporting Information, Figure S1). From the total particle mass change and the cholestane decay data, it is estimated that over 60% of the reaction products remain in the particle phase after 90% of the cholestane is consumed. OH oxidation likely occurs at the particle surface or near-surface region. This large cholestane depletion at higher OH exposures suggests either diffusion of OH into the subsurface region or, conversely, surface replenishment of cholestane from the interior of the particle.¹⁰ It cannot be ruled out that secondary chemistry might also deplete cholestane in the particle and the total loss of 90% is the sum of both secondary chemistry and the primary OH reaction at the particle surface.

It should be noted that, the cholestane mass remains unchanged beyond an OH exposure of 2×10^{12} molecules· $\text{cm}^{-3}\cdot\text{s}^{-1}$ indicating that $\sim 10\%$ of cholestane remains unreacted in the particles at the end of the experiment. This is approximately equivalent to a 100 nm diameter core of unreacted material inside a 200 nm diameter particle. The unreacted cholestane core that remains is likely due to either the short reacto-diffusive length of OH and/or the slow diffusion of cholestane from inside the particle to the surface. Additionally, it is also possible that the reaction rate of cholestane decreases with OH exposure (leading to the presence of an unreactive core) due to the saturation of surface reactive sites by species such as OH and/or O_3 .^{23,24} This offset exponential behavior has been reported in previous

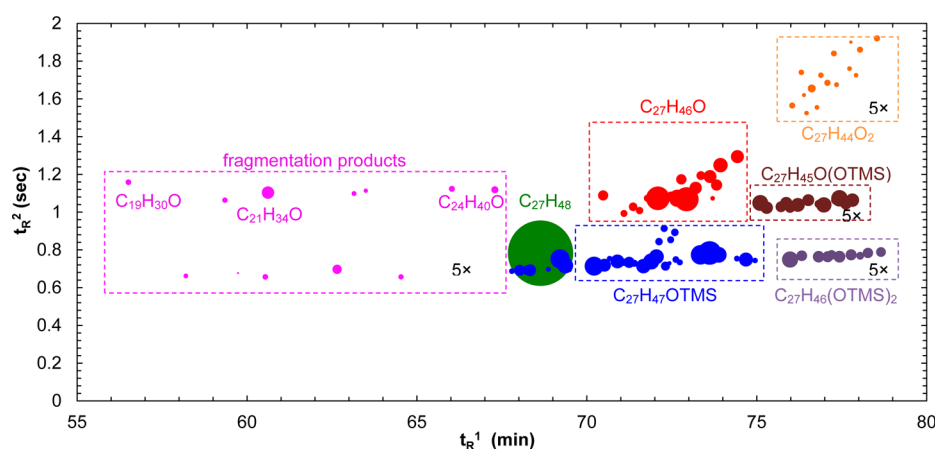


Figure 2. Cholestane oxidation product distribution shown in a 2D GC space (OH exposure = 2.5×10^{12} molecules· $\text{cm}^{-3}\cdot\text{s}^{-1}$). The x -axis is the first dimension (t_R^1) and the y -axis is the second dimension (t_R^2) retention time. Each circle represents a single compound and its relative abundance is represented by the size of the circle. Cholestane is the green circle located at $t_R^1 \sim 69$ min and $t_R^2 \sim 0.8$ s. The oxidation products are separated into six groups by their chemical formulas and delineated with different colors: all fragmentation products (pink); cholestanones and cholestanals ($\text{C}_{27}\text{H}_{46}\text{O}$, red); derivatized cholestanols ($\text{C}_{27}\text{H}_{47}\text{OTMS}$, blue); cholestadienes ($\text{C}_{27}\text{H}_{44}\text{O}_2$, orange); derivatized cholestadiols [$\text{C}_{27}\text{H}_{46}(\text{OTMS})_2$, purple]; and derivatized hydroxycholestanones [$\text{C}_{27}\text{H}_{45}\text{O}(\text{OTMS})$, brown]. The points corresponding to the fragmentation products and second-generation oxidation products (i.e., cholestadienes, cholestadiols, and hydroxycholestanones) are multiplied by a factor of 5.

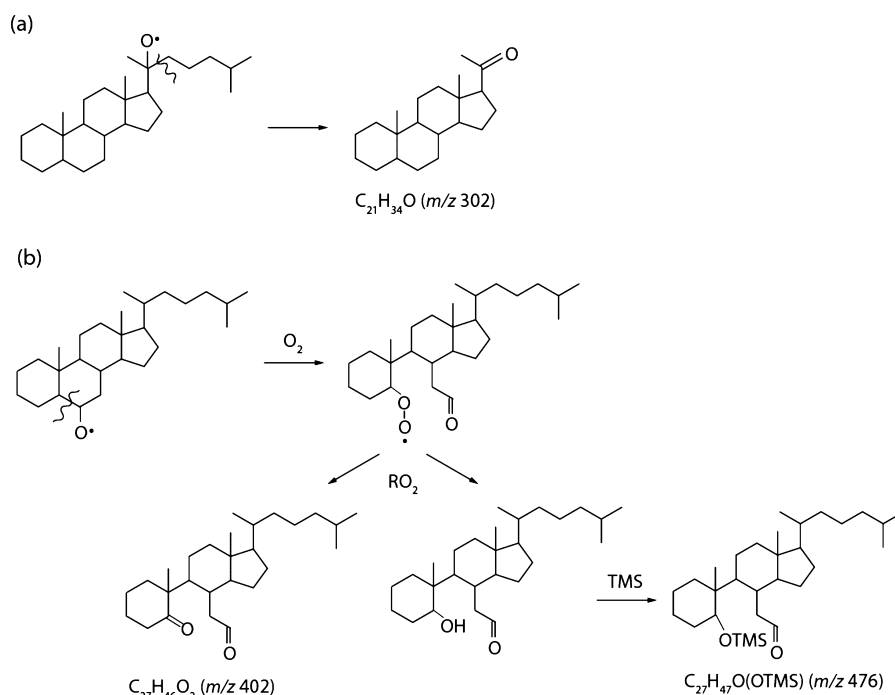


Figure 3. Examples of carbon–carbon bond cleavage on (a) aliphatic side chain and (b) rings of the androstane skeleton. In panel a, products of carbon bond cleavage on the side chain were also observed at the other two tertiary carbons (i.e., forming C_{19} and C_{24} carbonyls). Carbon bond cleavage products on the rings shown in panel b are found to be insignificant.

studies,^{10,19} suggesting that this effect is ubiquitous, especially for larger solid particles.

Effective uptake coefficients of OH reacting with cholestane are calculated from the cholestane decay rate:

$$\frac{dC}{dt} = -k_{\text{eff}}C[\text{OH}] \quad (1)$$

$$k_{\text{eff}} = -\frac{\ln(C_t/C_0)}{[\text{OH}]t} \quad (2)$$

where k_{eff} is the reaction effective rate coefficient. The ratio of cholestane concentration at time t (C_t) to initial concentration (C_0) is calculated from the chromatographic signals. $[\text{OH}]t$ is the OH exposure determined from the decay of the gas-phase tracer hexane. In the present study, the cholestane decay slows at higher oxidation levels (i.e., nonexponential) and hence cannot be represented by a single rate. Therefore, an “initial rate” method (a linear fit to the cholestane decay with OH exposure $< 2 \times 10^{12}$ molecules·cm^{−3}·s^{−1}) is used to estimate the uptake coefficient.¹⁹

The effective uptake coefficient (γ_{eff}), defined as the number of OH–cholestane collisions that yield a reaction, can be estimated by¹¹

$$\gamma_{\text{eff}} = \frac{4k_{\text{eff}}D_{\text{surf}}\rho N_A}{6\bar{c}M_w} \quad (3)$$

where k_{eff} is the “initial” cholestane decay rate calculated from eq 2; D_{surf} is the mean surface weighted diameter; ρ is the particle density (0.91 g·cm^{−3} for cholestane); N_A is Avogadro’s number; \bar{c} is the average speed of OH radicals in air (609.2 m·s^{−1}); and M_w is the molecular mass of cholestane (372.67 g·mol^{−1}). By use of these equations, the effective uptake coefficient of OH radicals reacting with cholestane is estimated

to be 0.49 ± 0.07 , which is consistent with the value reported in a previous study of motor oil oxidation.¹⁴

3.2. Oxidation Product Analyses. Figure 2 shows an example of the distribution and relative abundance of the cholestane oxidation products (OH exposure $\sim 2.5 \times 10^{12}$ molecules·cm^{−3}·s^{−1}) in two-dimensional GC space (i.e., t_R^1 vs t_R^2). The compounds that elute at earlier retention times than cholestane ($t_R^1 \sim 69$ min) are more volatile compounds (but still in the particle phase, given the high particle loadings in the flow tube). In this case, fragmentation products have carbon numbers less than 27. Likewise, the compounds that elute at longer t_R^1 relative to cholestane are functionalization products (i.e., carbon number = 27 with new oxygenated functional groups). The total abundance of the functionalization products is much larger than that of the fragmentation products. Vacuum UV photoionization mass spectrometry, which exhibits a more pronounced parent ion signal and less fragment ions relative to traditional EI, was used to identify the chemical formula of the oxidation products.²⁰ The EI mass spectra were also used to identify the structural positions of functional groups.

The molecular formulas of the oxidation products were determined from the high-resolution VUV mass spectrometry results, but for simplicity only integer m/z values are shown, and they are grouped as shown in Figure 2. Seventeen cholestanone/cholestanal isomers ($C_{27}H_{46}O$, $M_w = 386$, shown in red) and 23 trimethylsilyl (TMS)-derivatized cholestanol isomers ($C_{27}H_{47}OTMS$, $M_w = 460$, shown in blue) were detected as the main first-generation functionalization products. The TMS derivatization decreases the polarity of the alcohol molecules so that the second-dimension retention times were shorter than those of the cholestanones/cholestanals. In addition to these products, some unsaturated isomers (cholestenes, $C_{27}H_{46}$, $M_w = 370$) are also detected and shown in Figure 2 with t_R^1 from 67 to 70 min. Since the OH and ozone concentrations were high during the flow tube

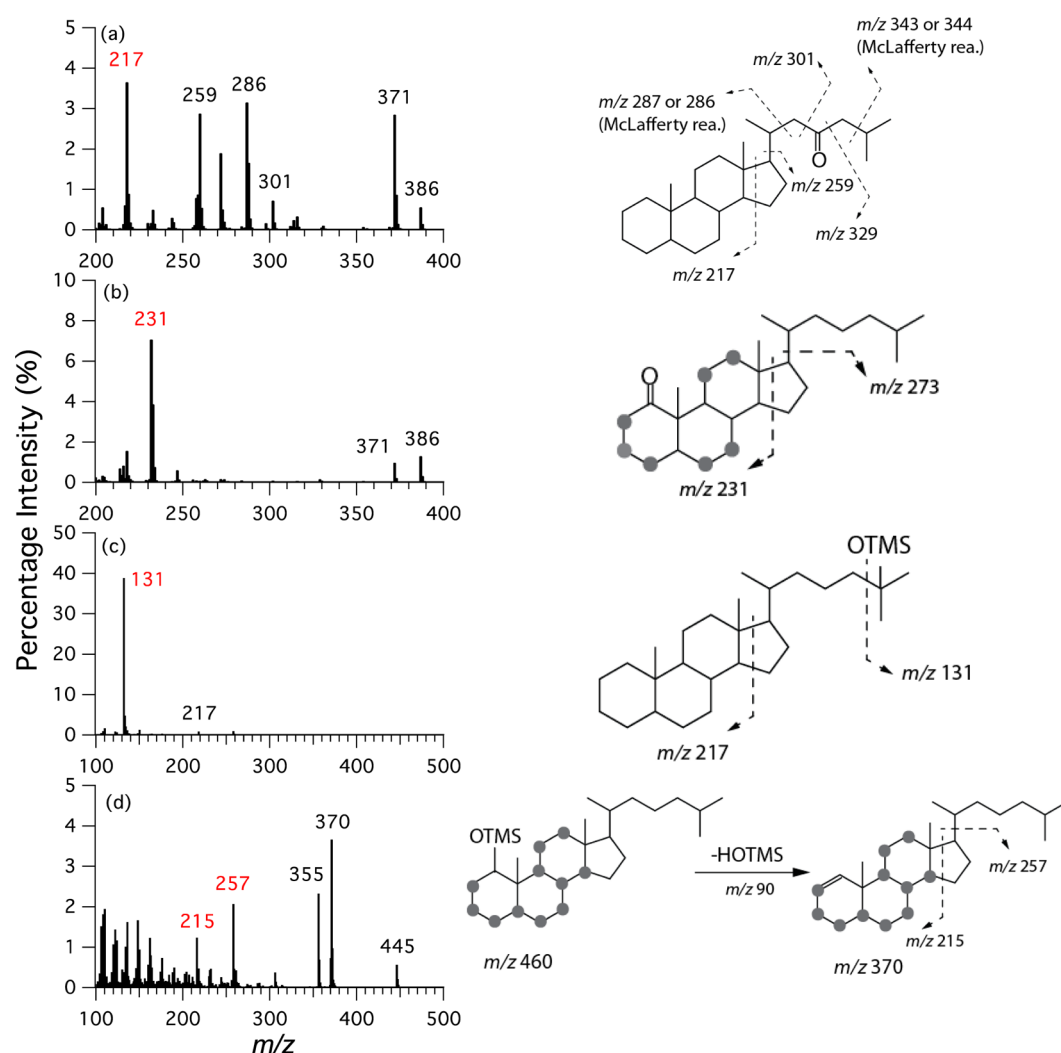


Figure 4. Representative examples of EI mass spectra, showing the main ion fragments: (a) carbonyl group on aliphatic side chain, (b) carbonyl group on cyclohexane rings, (c) hydroxyl group on aliphatic side chain, and (d) hydroxyl group on cyclohexane rings. Gray dots show possible locations of functional groups. Ion fragmentation patterns, which explain the dominant features observed in the mass spectra, are also shown in the figure.

experiments, it is unlikely that cholestene, if formed by the reaction, would remain in the aerosol. Rather, the cholestene isomers observed in the chromatogram are more likely formed from cholesterol dehydration during the GC thermal desorption process as discussed in Ruehl et al.²¹ Hence, they are grouped with cholesterol and shown in blue in Figure 2.

Oxidation products containing two oxygenated functional groups on each molecule were also detected, although at much lower abundances. These products include cholestadienes ($C_{27}H_{44}O_2$, $M_w = 400$), cholestadiols [derivatized formula: $C_{27}H_{46}(OTMS)_2$, $M_w = 548$], and hydroxycholestanones [derivatized formula: $C_{27}H_{45}O(OTMS)$, $M_w = 474$]. Higher-generation products (those with three or more oxygen atoms per molecule) were not observed and appear to contribute to a small fraction of the total detected aerosol mass. Though these higher polarity molecules will have reduced transmission efficiency through the GC column, their low abundance is consistent with the overall kinetic evolution of the first-generation products (precursors for higher product generations), shown in Figure 1, whose concentration remains unchanged at the end of the reaction rather than being consumed to produce higher-generation oxidation products. It

should also be noted that carboxylic acid products ($[M - C(O)OTMS]^+$ in EI mass spectrum) are not observed here, which is in contrast to results from Ruehl et al.,²¹ where carboxylic acid products were observed from *n*-octacosane (straight-chain) oxidation but not for squalane (branched-chain) oxidation. In this respect, the oxidation of cholesterol is more similar to that of branched alkanes.

Carbon bond cleavage can occur on both the side chain (example shown in Figure 3a) and the aliphatic rings (example shown in Figure 3b), forming fragmentation and ring-opening products, respectively. The observed fragmentation products in the particle phase are all molecules that have 19 or more carbons, which is consistent with fragmentation reactions occurring primarily on the eight-carbon aliphatic side chain. The most abundant fragmentation products are C_{24} , C_{21} , and C_{19} ketones ($C_{24}H_{40}O$, $C_{21}H_{34}O$, and $C_{19}H_{30}O$). These products all form from carbon bond cleavage at the tertiary carbons on or connecting the aliphatic side chain to the rings of the androstane skeleton (see detailed mechanism in Figure S2, Supporting Information), suggesting that alkoxy radical decomposition occurs primarily on these tertiary carbon sites on the aliphatic side chain. The total mass of the fragmentation

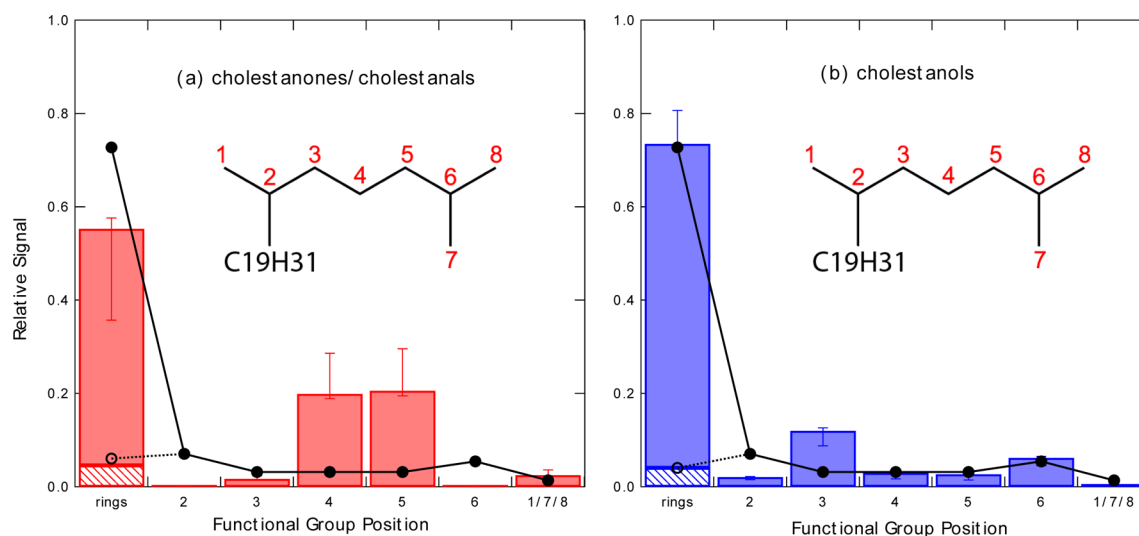


Figure 5. Relative abundance of (a) cholestanone/cholestanal and (b) cholestanol positional isomers. The black line shows gas-phase structure–reactivity relationship (SRR) predictions for relative hydrogen abstraction rates, in which rings are favored because they contain the majority of carbon atom reactive sites. The relative fractions of functional isomers on the rings normalized to the total number of available carbon sites and corresponding SRR predictions are also shown as dashed bars. Error bars represent the different fractions of positional isomers under different OH exposure conditions.

products in the particle phase accounts for less than 5% of total speciated mass. Given the high aerosol mass loading in the flow tube experiments, these particle-phase fragmentation products likely have even lower fractions under more atmospheric-relevant conditions. In previous studies of secondary organic aerosol (SOA) formation, ring-opening products were proposed to form and explain the higher SOA yield from the oxidation of cyclic compounds.^{5,6,25} However, in the present work, ring-opening products from cholestane [i.e., $C_{27}H_{46}O_2$ and $C_{27}H_{47}O(OTMS)$, Figure 3b] are found to be insignificant compared to the other bifunctional products (Figure S3, Supporting Information). Possible explanations for this observation will be discussed in more detail in section 3.4.

Figure 1 shows the normalized mass concentrations of the main oxidation products as a function of OH exposure. The data reveal that the carbonyl and the hydroxyl products are formed in very similar yields throughout the reaction and account for up to 50% of the total aerosol mass. The overall particle-phase fragmentation products (e.g., $C_{21}H_{34}O$) account for a much smaller fraction (<5%). The absolute mass closure for unreacted cholestane is $91\% \pm 5\%$, suggesting the overall mass closure from the TD-GC \times GC/ELVUV-HR-TOFMS analysis at all OH exposures is likely over 60% (with errors due to uncertainties in quantifying all the observed products). The remaining missing mass is probably due to evaporated reaction products (i.e., volatilization) in addition to more highly oxygenated (with more than three oxygen atoms in a molecule) particle-phase species that have low detection efficiency (i.e., polar compounds). Although the kinetic evolution of the products does not follow a sequential or statistical oxidation pattern,¹¹ which is characteristic of a well-mixed liquid particle, the product formation kinetics are consistent with the cholestane decay (i.e., products reached plateau when cholestane decay rate slowed). Future work is required to fully examine how aerosol phase state impacts product formation kinetics.

3.3. Distribution of Positional Isomers. By use of high-resolution mass spectra, the locations of the oxygen functional groups on the cholestane carbon backbone can be further

resolved.²¹ However, unlike the straight- or branched-chain compounds, the structural isomers on the rings of the androstane skeleton have very similar mass spectral signatures. Therefore, it is only possible to distinguish isomers formed on the rings from those formed on the aliphatic side chain. In the discussion below, all formulas are determined by the exact mass of the ions, but for simplicity only integer m/z values are shown.

Figure 4 shows representative examples of EI mass spectra of carbonyls and alcohols formed on the rings and side chain (VUV mass spectra are shown in Figure S4, Supporting Information). The ion fragmentation schemes that explain the main features of the mass spectra are also included in Figure 4. From analysis of both the EI and VUV mass spectra, the typical fragment ion of cholestane is m/z 217 ($C_{16}H_{25}^+$) (see Figure S1 in Supporting Information), suggesting that, upon ionization, dissociation occurs at the C–C bonds connecting the cyclopentane ring to the cyclohexane ring. The first-generation functionalization products of cholestane (i.e., carbonyls and alcohols) inherit this feature. For cholestanone/cholestanal isomers, m/z 217 is a major fragment ion when the carbonyl group is located either on the side chain (Figure 4a) or the pentane ring. When this occurs, α -cleavage, β -cleavage, and McLafferty rearrangements produce a number of fragment ions that can be used to ascertain the position of the carbonyl group, as shown in Figure 4a. For example, m/z 301 is a fragment ion from α -cleavage, while m/z 286 is a fragment produced by McLafferty rearrangement. The tertiary C–C bond connecting the rings to the side chain is weakened by the nearby carbonyl and thus m/z 259 is observed in some mass spectra. m/z 371 ($[M - CH_3]^+$) is also inherited from cholestane and thus shown as a main fragment. Its relative abundance varies with different isomers. When a carbonyl group is formed on one of the cyclohexane rings, m/z 231 ($C_{16}H_{23}O^+$) is the major fragment in the mass spectra (Figure 4b). The ordinary α -cleavage, β -cleavage, and McLafferty rearrangement on rings do not produce smaller fragment ions. Since this mass spectrum has fewer fragments, as shown in Figure 4b, far less information

is available in order to resolve the positional isomers formed on the rings of cholestane.

For TMS-derivatized cholestanol isomers, α -cleavage and loss of "HOTMS" (similar to dehydration of alcohols) are the normal fragment patterns. Figure 4c shows an example of TMS-derivatized cholestanol isomer with a functional group on the side chain. α -Cleavage is the dominant fragmentation pathway producing m/z 131 ($C_3H_6OTMS^+$) in this case. If the functional group is located on a side-chain position, α -cleavage produces fragment ions with formula $C_nH_{2n}OTMS^+$ ($n = 3-6$ and 8, corresponding to m/z 131, 145, 159, 173, and 201) and $[M - C_nH_{2n+1}]^+$ ($n = 4-6$, corresponding to m/z 403, 389, and 375). Alternatively, if the OTMS group is located on the cyclohexane rings, as shown in Figure 4d, then α -cleavage does not produce a new fragment ion and the major fragment is simply $[M - HOTMS]^+$. Under such a condition, m/z 215 ($C_{16}H_{23}^+$) and 257 ($C_{19}H_{29}^+$) are the main fragment ions.

The ketones and alcohols on the pentane ring can be determined by the same method (see examples in Figure S5, Supporting Information). In contrast to functional groups on the hexane rings, m/z 217 will appear instead of m/z 231 (ketones) or m/z 215 (alcohols). In addition, the other fragment ions from either McLafferty rearrangement (for ketones) or double-bond formation (for alcohols) can help determine the isomers on the pentane ring.

Using the approach discussed above, the distributions of cholestanone/cholestanal and cholestanol structural isomers are resolved and shown in Figure 5. In both cases, the functional groups are mostly formed on the rings, since there are more possible carbon reactive sites (i.e., 12 out of 18 possible sites for carbonyls and 16 out of 24 possible sites for alcohols). Overall, the cholestanone/cholestanal isomers located on the rings account for about 55% of the total isomers. In contrast, for cholestanols, ring isomers account for 74% of total cholestanol isomers. Figure 5 shows the relative fractions of isomers on the rings normalized by the total number of available carbon sites for either carbonyl or alcohol formation. On average, individual carbonyl isomers on the rings are much less abundant compared to the ketones on chain positions 4 and 5, which are enhanced compared to the other side-chain isomers. In contrast, the alcohol isomers are enriched on carbon positions 3 and 6 on the side chain, where tertiary carbon atoms are located.

Included in Figure 5 are the structure–reactivity relationship (SRR) predictions for the relative hydrogen abstraction rates from each carbon site, derived from previous gas-phase studies.²⁶ The averaged relative hydrogen abstraction rate for carbon atoms on the rings is also shown. The general trend of the positional isomer distribution follows somewhat the SRR predictions of gas-phase H-abstraction rates. However, more carbonyls are observed at positions 4 and 5 on the side chain than predicted by SRR. Additionally, fewer carbonyls and alcohols are observed on carbon position 2 than the SRR prediction, which is likely due to C–C bond scission on the tertiary carbon, which will be discussed in detail in section 3.4.

3.4. Discussion of Potential Oxidation Mechanism.

Figure 6 illustrates the main heterogeneous OH oxidation pathways of cholestane in the absence of nitrogen oxides, based upon previous studies.^{2,9} Other possible reactions such as peroxy radicals (RO_2) + HO_2 are not shown since products of these reaction pathways are not observed and the high OH concentrations used here favor instead RO_2 + RO_2 reactions. It should be noted that in the ambient atmosphere RO_2 + HO_2

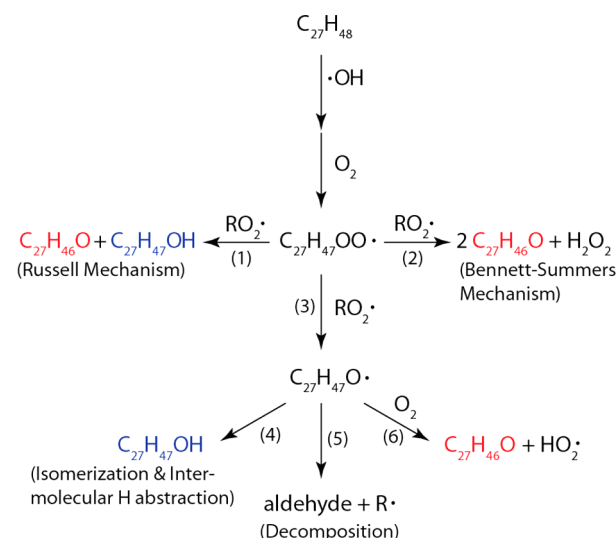


Figure 6. Generalized reaction scheme for the heterogeneous oxidation of cholestane by OH radicals in the presence of O_2 .

could be the main reaction pathway due to the high abundance of HO_2 radicals.

In the gas phase, the branching ratio for RO_2 + RO_2 reactions is $\sim 0.3-0.8$ to form stable products via pathway 1 (ketone and alcohol), with the remaining fraction split between pathway 3 to alkoxy radical formation²⁷ and pathway 2 to carbonyl formation. In the present work, cholestanones/cholestanals and cholestanols are identified as the major products, which could result from pathway 1, known as the Russell mechanism in the condensed phase.²⁸ Alternatively, it could also be explained by an equal split between pathways 4 (alcohol formation) and 6 (ketone formation) from alkoxy radicals. In previous heterogeneous oxidation studies, carbonyls have been consistently detected in larger abundance than alcohols,^{9,10,29,30} highlighting the possible contribution of the Bennett–Summers mechanism (pathway 2) as well as the alkoxy radical reaction with oxygen (pathway 6), both of which form carbonyls. The Bennett–Summers pathway usually occurs at low temperatures;³¹ however, H_2O_2 has been detected in a previous study at room temperature,²⁹ suggesting it is possible that this mechanism may play a role in a surface reaction. Hearn et al.²⁹ observed the relative abundance of carbonyls to alcohols to increase with increasing O_2 mixing ratio, suggesting the importance of pathway 6. For cholestane oxidation, the alcohol/carbonyl ratio (~ 1) is higher than observed in previous work (< 1), indicating that additional pathways that form alcohols (i.e., isomerization resulting from either intermolecular or intramolecular hydrogen abstractions) might also contribute to the overall mechanism.

An alkoxy radical can abstract a hydrogen atom from either itself (intramolecular isomerization) or a nearby molecule (intermolecular H abstraction) to form an alcohol. For intramolecular isomerization, the alcohol molecule with an alkyl radical will likely react with oxygen and form a hydroxyl peroxy radical, which undergoes further reactions to produce either a hydroxyl carbonyl or a diol. Here we find that for the cholestane oxidation products with two oxygen atoms per molecule, hydroxycholestanones and cholestadiols, are more abundant than cholestadiones by factors of ~ 5 and ~ 3 (Figure S6, Supporting Information), respectively. This suggests that at least some of these hydroxyl-group-containing bifunctional

products might originate from either alkoxy radical isomerization or intermolecular H abstraction.

Among cholestane's 25 unsaturated carbons, 5 are primary, 13 are secondary, and 7 are tertiary carbons. Hydrogen abstraction rates estimated by SRR²⁶ suggest that about 56% of the cholestane RO₂ would be formed on tertiary carbons, with 42% and 2% formed at secondary- and primary-carbon sites, respectively. Pathway 1 in Figure 5 does not occur for the self-reaction of two tertiary-carbon RO₂ radicals,³² which instead react to form two alkoxy radicals (pathway 3). Since 56% of cholestane RO₂ radicals are tertiary, the probability of tertiary RO₂ + tertiary RO₂ is ~30% (if it is assumed all RO₂ + RO₂ rate constants are the same regardless of the difference between isomers). For the remaining RO₂ + RO₂ reactions, which do not involve two tertiary RO₂ (probability ~70%), the Russell mechanism is likely the dominant reaction pathway. If it is assumed that the branching ratio for the Russell mechanism is 0.8 (the upper bound for gas-phase RO₂ + RO₂ reactions) and equal for the Bennett–Summers as well as the alkoxy radical pathway (i.e., both 0.1), the alkoxy radical formation yield is estimated to be 37%, most of which are tertiary alkoxy radicals (see detailed calculation in Figure S7, Supporting Information). If the branching ratio to Russell mechanism is smaller than 0.8, the relative yield of alkoxy radicals will of course be larger.

Based on the SRR calculations, alkoxy radical chemistry appears to play a larger role in cholestane oxidation than it does for straight or even branched hydrocarbons due to the large fraction of tertiary carbon atoms in the molecule. The large difference in positional distributions between carbonyls and alcohols may be also due to the influence of alkoxy radical reactions. Primary and secondary alkoxy radicals mostly undergo pathways 4 and 6, forming alcohol and carbonyls. Alternatively, the tertiary alkoxy radicals can react only by pathways 4 and 5, producing alcohols and β -scission products.

For alkoxy radicals on the rings, β -scission would likely yield ring-opening products. However, ring-opening products are observed to be insignificant in cholestane oxidation (Figure S3, Supporting Information). This could be due in part to the low ring-strain energy on the hexane rings.³³ Lim and Ziemann⁵ reported that when ring-strain energy is low, the decomposition of cyclic alkane alkoxy radicals is inhibited. Thus the minor ring-opening products observed in Figure S3 most likely originate from the cyclopentane ring, which has higher ring-strain energy relative to the cyclohexane rings. Another possible reason for the low abundance of ring-opening products is that most of the ring alkoxy radicals are tertiary alkoxy radicals, which would produce energetically less stable primary alkyl radicals upon ring opening. This suggests that most ring tertiary alkoxy radicals form alcohols, which potentially explains why, in this study, alcohols and carbonyls are observed in equal abundance, in contrast to previous work that reported a larger carbonyl fraction.^{9,10,29,30} This is also consistent with the fact that ring alcohols are more abundant than ring carbonyls, as shown in Figure 5. However, the lower transfer efficiency at higher t_R ¹ may have caused an underestimate of ring-opening products to some extent.

Functional isomers at the primary carbon sites on the aliphatic side chain (positions 1, 7, and 8) are formed with low probability, which is consistent with SRR gas-phase predictions³⁴ as well as a recent heterogeneous oxidation study of normal and branched alkane aerosols.²¹ For secondary carbons on the side chain (positions 3, 4, and 5, Figure 4), the SRR predictions indicate similar hydrogen abstraction rates.

However, at positions 4 and 5 ketone formation is observed to be enhanced, while position 3 forms more alcohol than the gas-phase predictions. Isomerization of alkoxy radicals proceeds typically through a six-membered cyclic transition state.^{18,35} Based upon the structure of cholestane, alkoxy radicals on position 3 can potentially abstract one hydrogen atom from a tertiary carbon and two hydrogen atoms from a secondary carbon as shown in Figure S8 (Supporting Information). In contrast, alkoxy radicals on position 4 can abstract one hydrogen atom from a tertiary carbon and nine hydrogen atoms from three primary carbons. Alkoxy radicals on position 5 can abstract one hydrogen atom from one tertiary carbon. Thus, according to the isomerization hydrogen abstraction rates based upon Atkinson³⁵ for gas-phase alkoxy radicals, alkoxy radicals on position 3 can abstract hydrogen faster and hence this position is more favored to form alcohols, while alkoxy radicals located on carbon positions 4 and 5 preferentially react with O₂ to form ketones.

For the tertiary carbon sites on the side chain (position 2 and 6) where carbonyls cannot form, alcohols or, less likely, fragmentation products are possible. The speciation of fragmentation products suggests that C–C bond scission occurs more readily at position 2 (C₂₁H₃₄O more abundant than C₂₄H₄₀O) than at position 6, where alcohol formation is dominant. Although SRR predictions suggest similar hydrogen abstraction rates on these two tertiary sites (2 and 6), the final product distribution is controlled by subsequent chemistry of the RO₂ and alkoxy radical intermediates.

4. CONCLUSIONS

This work investigated the OH-initiated photochemical oxidation of cholestane aerosol at OH exposure up to 4×10^{12} molecules·cm⁻³·s⁻¹. The kinetic results suggest that approximately 10% of total cholestane remains unreacted even at high OH exposure. This implies the OH oxidation of cholestane mainly occurs at the near-surface region but some surface refreshment of cholestane occurs. However, the cholestane molecules in the inner core are not available for reaction with OH. This is likely due to short reacto-diffusive length of OH and/or slow diffusion of cholestane from the interior of the particle to the surface. The uptake coefficient for OH reacting with cholestane is estimated to be 0.49 ± 0.07 , consistent with a previous motor oil oxidation study.¹⁴

The gas chromatography/mass spectrometry results show that particle-phase fragmentation products and second-generation functionalization products are much less abundant than the first-generation functionalization products, which are identified as cholestanone/cholestanal (addition of a carbonyl group) and cholestanol (addition of a hydroxyl group) isomers. Interestingly, the cholestanones/cholestanals and cholestanols are formed in very similar concentrations over the whole OH exposure range. However, the positional distributions of cholestanones/cholestanals and cholestanols are different, suggesting the importance of alkoxy radicals and their chemistry at different carbon sites within the molecule. For example, tertiary alkoxy radicals tend to undergo mainly isomerization on the rings, forming cholestanols, and undergo both isomerization and decomposition on the side chain, forming cholestanols and fragmentation products, respectively. In contrast, the other alkoxy radicals (mostly secondary) appear to mainly react with oxygen or undergo isomerization.

Cyclic hydrocarbons, including hopanes and other steranes, have similar structure to cholestane with a large fraction of

tertiary carbon atoms. Hence, during their oxidation, most of the RO₂ are tertiary-carbon radicals (if the hydrogen abstraction rates by OH for different carbon atoms are assumed to be similar to those in the gas phase). These tertiary RO₂ undergo self-reactions, only they form alkoxy radicals (pathway 1 in Figure 5 is not accessible). Thus for these cyclic compounds, tertiary alkoxy radical chemistry is expected to play a substantial role in governing both the functionalization (alkoxy radicals isomerization and reaction with oxygen) and the fragmentation products (alkoxy radical decomposition). It is also noteworthy that ring-opening functionalization products were not observed in this study. It could be explained by the low ring-strain energies of the hexane rings and the pentane ring in cholestane. By analogy, ring-opening products are also expected to be unlikely for hopanes and other steranes. The results in this study highlight the important differences in photochemical oxidation mechanisms between cyclic alkanes and their branched and normal analogues.

■ ASSOCIATED CONTENT

■ Supporting Information

Additional text describing estimation of oxidized particle density and eight figures showing sample mass spectra of oxidation products; formation mechanisms of main fragmentation products; molecular ion vs 1D retention time; samples of VUV mass spectra of CO and OH groups on side chain and hexane and pentane rings; relative fractions of cholestane bifunctional products; fractions of RO₂ + RO₂ reaction pathways; and decomposition of alkoxy radicals via isomerization. This material is available free of charge via the Internet at <http://pubs.acs.org>.

■ AUTHOR INFORMATION

Corresponding Author

*E-mail krwilson@lbl.gov; tel 1-510-495-2474.

Present Address

Department of Chemical Engineering and Applied Chemistry, University of Toronto, Toronto, Ontario M5S 3E5, Canada.

Notes

The authors declare no competing financial interest.

■ ACKNOWLEDGMENTS

This work was supported by the Laboratory-Directed Research and Development (LDRD) Program of Lawrence Berkeley National Laboratory under U.S. Department of Energy Contract DE-AC02-05CH11231. K.R.W. and C.R.R. are supported by the Department of Energy, Office of Science, Early Career Research Program.

■ REFERENCES

- (1) Hallquist, M.; Wenger, J. C.; Baltensperger, U.; Rudich, Y.; Simpson, D.; Claeys, M.; Dommen, J.; Donahue, N. M.; George, C.; Goldstein, A. H.; et al. The Formation, Properties and Impact of Secondary Organic Aerosol: Current and Emerging Issues. *Atmos. Chem. Phys.* **2009**, *9*, 5155–5236.
- (2) George, I. J.; Abbatt, J. P. D. Heterogeneous Oxidation of Atmospheric Aerosol Particles by Gas-phase Radicals. *Nat. Chem.* **2010**, *2*, 713–722.
- (3) Kroll, J. H.; Donahue, N. M.; Jimenez, J. L.; Kessler, S. H.; Canagaratna, M. R.; Wilson, K. R.; Altieri, K. E.; Mazzoleni, L. R.; Wozniak, A. S.; Bluhm, H.; et al. Carbon Oxidation State as a Metric

for Describing the Chemistry of Atmospheric Organic Aerosol. *Nat. Chem.* **2011**, *3*, 133–139.

- (4) Wilson, K. R.; Smith, J. D.; Kessler, S. H.; Kroll, J. H. The Statistical Evolution of Multiple Generations of Oxidation Products in the Photochemical Aging of Chemically Reduced Organic Aerosol. *Phys. Chem. Chem. Phys.* **2012**, *14*, 1468–1479.

- (5) Lim, Y. B.; Ziemann, P. J. Effects of Molecular Structure on Aerosol Yields from OH Radical-initiated Reactions of Linear, Branched, and Cyclic Alkanes in the Presence of NO_x. *Environ. Sci. Technol.* **2009**, *43*, 2328–2334.

- (6) Lambe, A. T.; Onasch, T. B.; Croasdale, D. R.; Wright, J. P.; Martin, A. T.; Franklin, J. P.; Massoli, P.; Kroll, J. H.; Canagaratna, M. R.; Brune, W. H.; et al. Transitions from Functionalization to Fragmentation Reactions of Laboratory Secondary Organic Aerosol Generated from the OH Oxidation of Alkane Precursors. *Environ. Sci. Technol.* **2012**, *46*, 5430–5437.

- (7) Yee, L. D.; Craven, J. S.; Schilling, K. A.; Ng, N. L.; Canagaratna, M. R.; Ziemann, P. J.; Flagan, R. C.; Seinfeld, J. H. Effect of Chemical Structure on Secondary Organic Aerosol formation for C₁₂ Alkanes. *Atmos. Chem. Phys. Discuss.* **2013**, *13*, 10859–10903.

- (8) Hearn, J. D.; Smith, G. D. Measuring Rates of Reaction in Supercooled Organic Particles with Implications for Atmospheric Aerosol. *Phys. Chem. Chem. Phys.* **2005**, *7*, 2549–2551.

- (9) George, I. J.; Vlasenko, A.; Slowik, J. G.; Broekhuizen, K.; Abbatt, J. P. D. Heterogeneous Oxidation of Saturated Organic Aerosols by Hydroxyl Radicals: Uptake Kinetics, Condensed-phase Products, and Particle Size Change. *Atmos. Chem. Phys.* **2007**, *7*, 4187–4201.

- (10) McNeill, V. F.; Yatavelli, R. L. N.; Thornton, J. A.; Stipe, C. B.; Landgrebe, O. Heterogeneous OH Oxidation of Palmitic Acid in Single Component and Internally Mixed Aerosol Particles: Vaporization and the Role of Particle Phase. *Atmos. Chem. Phys.* **2008**, *8*, 5464–5476.

- (11) Smith, J. D.; Kroll, J. H.; Cappa, C. D.; Che, D. L.; Liu, C. L.; Ahmed, M.; Leone, S. R.; Worsnop, D. R.; Wilson, K. R. The Heterogeneous Reaction of Hydroxyl Radicals with Sub-micron Squalane Particles: a Model System for Understanding the Oxidative Aging of Ambient Aerosols. *Atmos. Chem. Phys.* **2009**, *9*, 3209–3222.

- (12) Lambe, A. T.; Miracolo, M. A.; Robinson, A. L.; Donahue, N. M. Effective Rate Constants and Uptake Coefficients for the Reactions of Organic Molecular Markers (*n*-Alkanes, Hopanes, and Steranes) in Motor Oil and Diesel Primary Organic Aerosols with Hydroxyl Radicals. *Environ. Sci. Technol.* **2009**, *43*, 8794–8800.

- (13) Kessler, S. H.; Smith, J. D.; Che, D. L.; Worsnop, D. R.; Wilson, K. R.; Kroll, J. H. Chemical Sinks of Organic Aerosol: Kinetics and Products of the Heterogeneous Oxidation of Erythritol and Levoglucosan. *Environ. Sci. Technol.* **2010**, *44*, 7005–7010.

- (14) Isaacman, G.; Chan, A. W. H.; Nah, T.; Worton, D. R.; Ruehl, C. R.; Wilson, K. R.; Goldstein, A. H. Heterogeneous OH Oxidation of Motor Oil Particles Causes Selective Depletion of Branched and Less Cyclic Hydrocarbons. *Environ. Sci. Technol.* **2012**, *46*, 10632–10640.

- (15) Lambe, A. T.; Zhang, J.; Sage, A. M.; Donahue, N. M. Controlled OH Radical Production via Ozone-Alkene Reactions for Use in Aerosol Aging Studies. *Environ. Sci. Technol.* **2009**, *41*, 2357–2363.

- (16) Weitkamp, E. A.; Lambe, A. T.; Donahue, N. M.; Robinson, A. L. Laboratory Measurements of the Heterogeneous Oxidation of Condensed-phase Organic Molecular Markers for Motor Vehicle Exhaust. *Environ. Sci. Technol.* **2008**, *42*, 7950–7956.

- (17) George, I. J.; Abbatt, J. P. D. Chemical Evolution of Secondary Organic Aerosol from OH-Initiated Heterogeneous Oxidation. *Atmos. Chem. Phys.* **2010**, *10*, 5551–5563.

- (18) Kroll, J. H.; Smith, J. D.; Che, D. L.; Kessler, S. H.; Worsnop, D. R.; Wilson, K. R. Measurement of Fragmentation and Functionalization Pathways in the Heterogeneous Oxidation of Oxidized Organic Aerosol. *Phys. Chem. Chem. Phys.* **2009**, *11*, 8005–8014.

- (19) Kessler, S. H.; Nah, T.; Daumit, K. E.; Smith, J. D.; Leone, S. R.; Kolb, C. E.; Worsnop, D. R.; Wilson, K. R.; Kroll, J. H. OH-Initiated Heterogeneous Aging of Highly Oxidized Organic Aerosol. *J. Phys. Chem. A* **2012**, *116*, 6358–6365.

(20) Isaacman, G.; Wilson, K. R.; Chan, A. W. H.; Worton, D. R.; Kimmel, J. R.; Nah, T.; Hohaus, T.; Gonin, M.; Kroll, J. H.; Worsnop, D. R.; et al. Improved Resolution of Hydrocarbon Structures and Constitutional Isomers in Complex Mixtures Using Gas Chromatography-Vacuum Ultraviolet-Mass Spectrometry. *Anal. Chem.* **2012**, *84*, 2335–2342.

(21) Ruehl, C. R.; Nah, T.; Isaacman, G.; Worton, D. R.; Chan, A. W. H.; Kolesar, K. R.; Cappa, C. D.; Goldstein, A. H.; Wilson, K. R. The Influence of Molecular Structure and Aerosol Phase on the Heterogeneous Oxidation of Normal and Branched Alkanes by OH. *J. Phys. Chem. A* **2013**, *117*, 3990–4000.

(22) Worton, D. R.; Isaacman, G.; Gentner, D. R.; Dallmann, T. R.; Chan, A. W. H.; Ruehl, C. R.; Krischetter, T. W.; Wilson, K. R.; Harley, R. A.; Goldstein, A. H. Unburned Lubricating Oil Dominates Primary Organic Particulate Emissions from Motor Vehicle Exhaust. Manuscript in preparation, 2013

(23) Renbaum, L. H.; Smith, G. D. Artifacts in Measuring Aerosol Uptake Kinetics: the Roles of Time, Concentration and Adsorption. *Atmos. Chem. Phys.* **2011**, *11*, 6881–6893.

(24) Slade, J. H.; Knopf, D. A. Heterogeneous OH Oxidation of Biomass Burning Organic Aerosol Surrogate Compounds: Assessment of Volatilisation Products and the Role of OH Concentration on the Reactive Uptake Kinetics. *Phys. Chem. Chem. Phys.* **2013**, *15*, 5898–5915.

(25) Tkacik, D. S.; Presto, A. A.; Donahue, N. M.; Robinson, A. L. Secondary Organic Aerosol Formation from Intermediate-volatility Organic Compounds: Cyclic, Linear, and Branched Alkanes. *Environ. Sci. Technol.* **2012**, *46*, 8773–8781.

(26) Kwok, E. S.; Atkinson, R. Estimation of Hydroxyl Radical Reaction-rate Constants for Gas-phase Organic-Compounds Using a Structure-Reactivity Relationship: an Update. *Atmos. Environ.* **1995**, *29*, 1685–1695.

(27) Atkinson, R. Gas-phase Tropospheric Chemistry of Volatile Organic Compounds. 1. Alkanes and Alkenes. *J. Phys. Chem.* **1997**, *26*, 215–290.

(28) Russell, G. A. Deuterium-isotope Effect in the Autoxidation of Alkyl Hydrocarbons. Mechanism of the Interaction of Peroxy Radicals. *J. Am. Chem. Soc.* **1957**, *79*, 3871–3877.

(29) Hearn, J. D.; Renbaum, L. H.; Wang, X.; Smith, G. D. Kinetics and Products from Reaction of Cl Radicals with Dioctyl Sebacate (DOS) Particles in O₂: a Model for Radical-initiated Oxidation of Organic Aerosols. *Phys. Chem. Chem. Phys.* **2007**, *9*, 4803–4813.

(30) Renbaum, L. H.; Smith, G. D. The Importance of Phase in the Radical-initiated Oxidation of Model Organic Aerosols: Reactions of Solid and Liquid Brassidic Acid Particles. *Phys. Chem. Chem. Phys.* **2009**, *11*, 2441–2451.

(31) Bennett, J. E.; Summers, R. Product Studies of the Mutual Termination Reactions of *sec*-alkylperoxy Radicals: Evidence for Non-cyclic Termination. *Can. J. Chem.* **1974**, *52*, 1377–1379.

(32) Atkinson, R. Gas-phase Tropospheric Chemistry of Organic Compounds: a Review. *Atmos. Environ.* **1990**, *24A*, 1–41.

(33) Anslyn, E. V.; Dennis, A. D. Chapter 2: Strain and Stability. In *Modern Physical Organic Chemistry*; University Science: Sausalito, CA, 2006; pp 100–109.

(34) Atkinson, R. A Structure-Activity Relationship for the Estimation of Rate Constants for the Gas-phase Reactions of OH Radicals with Organic Compounds. *Int. J. Chem. Kinet.* **1987**, *19*, 799–828.

(35) Atkinson, R. Atmospheric Reactions of Alkoxy and β -Hydroxyalkoxy Radicals. *Int. J. Chem. Kinet.* **1997**, *29*, 99–111.